

# Phase-coherent transport in catalyst-free vapor phase deposited Bi<sub>2</sub>Se<sub>3</sub> crystals

R. Ockelmann<sup>1,2</sup>, A. Müller<sup>1</sup>, J. H. Hwang<sup>1</sup>, S. Jafarpisheh<sup>1,2</sup>, M. Drögeler<sup>1</sup>, B. Beschoten<sup>1</sup> and C. Stampfer<sup>1,2</sup>

<sup>1</sup>JARA-FIT and 2nd Institute of Physics, RWTH Aachen University, 52074 Aachen, Germany, EU

<sup>2</sup>Peter Grünberg Institute (PGI-9), Forschungszentrum Jülich, 52425 Jülich, Germany, EU

(Dated: April 19, 2022)

Free-standing Bi<sub>2</sub>Se<sub>3</sub> single crystal flakes of variable thickness are grown using a catalyst-free vapor-solid synthesis and are subsequently transferred onto a clean Si<sup>++</sup>/SiO<sub>2</sub> substrate where the flakes are contacted in Hall bar geometry. Low temperature magneto-resistance measurements are presented which show a linear magneto-resistance for high magnetic fields and weak anti-localization (WAL) at low fields. Despite an overall strong charge carrier tunability for thinner devices, we find that electron transport is dominated by bulk contributions for all devices. Phase coherence lengths  $l_\phi$  as extracted from WAL measurements increase linearly with increasing electron density exceeding 1  $\mu\text{m}$  at 1.7 K. While  $l_\phi$  is in qualitative agreement with electron-electron interaction-induced dephasing, we find that spin flip scattering processes limit  $l_\phi$  at low temperatures.

## I. INTRODUCTION

Topological insulators (TIs) are a new class of materials [1–5], consisting of an insulating bulk and *topologically protected* conducting surface states. These surface states are spin polarised and robust against scattering from non-magnetic impurities making them interesting candidates for future spintronics and quantum computing devices [6–8] as well as potential hosts for Majorana fermions [9–12]. Binary Bi-chalcogenides (Bi<sub>2</sub>Se<sub>3</sub>, Bi<sub>2</sub>Te<sub>3</sub>) belong to the class of three-dimensional (3D) strong topological insulators with a single Dirac cone at the surface [13] which is experimentally observable by angle-resolved photo emission spectroscopy [14]. In particular, Bi<sub>2</sub>Se<sub>3</sub> with a single Dirac cone centered in a bulk band gap of  $E_g \approx 350$  meV is a promising material for probing surface states by electronic transport. However, the measurement of pure surface states is challenging. So far Bi<sub>2</sub>Se<sub>3</sub> crystals are unintentionally *n*-type doped most likely by Se vacancies [15–17] leading to bulk conductivity dominating electronic transport. To increase the surface-to-bulk ratio, ultra-thin flakes with thickness of the order of 10 nm have been investigated [18].

Thin Bi<sub>2</sub>Se<sub>3</sub> crystals can be produced by mechanical exfoliation of bulk material as it is common practice for graphene fabrication [19, 20]. However, it is much more promising to grow thin Bi<sub>2</sub>Se<sub>3</sub> films in-situ which has been successfully achieved with molecular beam epitaxy (MBE) [21–23] or vapor-solid synthesis (VSS) in a tube furnace [18, 24, 25].

In this work, we show a catalyst free growth of large freestanding Bi<sub>2</sub>Se<sub>3</sub> flakes with a VSS method. Our free-standing growth approach ensures the synthesis of strain free, few-layer single crystal flakes with lateral dimensions up to 25  $\mu\text{m}$  and thicknesses in the range of 6 to 30 nm, ranking our flakes among the largest Bi<sub>2</sub>Se<sub>3</sub> single crystals flakes. The high structural and surface quality of the Bi<sub>2</sub>Se<sub>3</sub> crystals is verified by Raman and by scanning force microscopy. The free standing single crystals are ideal for transport studies. We utilize a wet chemistry-free process which allows transferring these single crystals onto any desired substrate with-

out introducing additional contamination. We studied low temperature magneto-transport on a series of Bi<sub>2</sub>Se<sub>3</sub> crystals of different thicknesses which were transferred on SiO<sub>2</sub>/Si<sup>++</sup> substrates. We observe linear magneto-resistance (LMR) at high *B*-fields as well as weak anti-localization (WAL) which both indicate the dominance of bulk transport contributions. Electron phase coherence lengths are in the micrometer range, slightly larger compared to earlier studies on Bi<sub>2</sub>Se<sub>3</sub> crystals grown directly on SiO<sub>2</sub> [26] or by other growth methods [27, 28]. We show that electron spin-flip processes limit the phase coherence length at low temperatures.

## II. CRYSTAL GROWTH AND CHARACTERISATION

With the goal of gaining high quality thin Bi<sub>2</sub>Se<sub>3</sub> crystals we applied a catalyst-free vapor-solid synthesis method. Most commonly, MBE [29–31] is used to grow thin films since it offers the growth of extended films of rich chemical compositions with excellent thickness control. Yet it suffers (i) from poly-crystallinity of the film inducing strain at the grain boundaries and (ii) from a limited number of usable substrates. In contrast to MBE, VSS allows the growth of single crystalline platelets on a variety of different substrates [32–34]. However, strain can still be induced by the growth substrate. Moreover, growth catalyst may induce unwanted dopants into the crystal. In this work we therefore use a catalyst-free VSS method where flakes and ribbons grow free standing on the substrate. This offers an interesting pathway for the fabrication of high quality devices. Free standing flakes are neither strained nor contaminated by the substrate material and can be easily transferred onto on a wide range of different substrates.

A standard three zone tube-furnace (Fig. 1(a)) with electric heating coils is used for the VSS growth. As a source material we place Bi<sub>2</sub>Se<sub>3</sub> crystals [35] in the first zone. The Si/SiO<sub>2</sub> growth substrates are placed downstream in the second zone. Their exact position was optimized through several growth cycles. Prior to growth,

the quartz tube was evacuated to 2 mbar with subsequent argon flushing for 5 min with 500 sccm flow rate which is regulated by a digital mass flow controller. After cleaning, the growth zone (second zone) is heated up to 325°C with a constant argon flow of 100 sccm to carry away vaporized particles. The second zone is kept at 325°C and 25 mbar for 2 h as it is crucial for the temperature and pressure to be stabilized during growth. Finally, the actual growth process is executed by heating the first zone to 700°C. The source material gradually vaporizes and gets carried downstream by an 60 sccm argon flow. Temperature and pressure were optimized to grow large, thin, free standing  $\text{Bi}_2\text{Se}_3$  flakes and ribbons as shown by scanning electron microscope (SEM) images in Figs. 1(b)-(d) and by atomic force microscope (AFM) images in Figs. 1(e)-(g). Straight edges with only 60° and 120° corners indicate single crystalline growth. According to AFM measurements the flake thicknesses range between 6 nm and 40 nm and lateral dimensions can reach up to 25  $\mu\text{m}$ . AFM images also reveal the flake's surfaces to be stepless confirming a very homogeneous layer by layer growth.

Raman spectroscopy has emerged as an excellent tool to probe crystal stoichiometry of  $\text{Bi}_2\text{Se}_3$  [36–38]. The Raman spectra of our  $\text{Bi}_2\text{Se}_3$  flakes is obtained using confocal Raman spectroscopy with a laser spot diameter of around 500 nm at a wavelength of 532 nm. The laser spot is precisely positioned on the flakes using a piezo stage. In Fig. 1(h) all four characteristic Raman peaks of  $\text{Bi}_2\text{Se}_3$  are clearly seen at 37  $\text{cm}^{-1}$ , 71  $\text{cm}^{-1}$ , 131  $\text{cm}^{-1}$  and 175  $\text{cm}^{-1}$ , which correspond to the  $E_g^1$ ,  $A_{1g}^1$ ,  $E_g^2$  and  $A_{1g}^2$  vibrational modes, respectively. The peak positions are very close to previously measured Raman peaks of stoichiometric  $\text{Bi}_2\text{Se}_3$  crystals [36, 39, 40] indicating the high crystal quality of our flakes.

For transport studies, the free standing  $\text{Bi}_2\text{Se}_3$  flakes are dry-transferred by gently dabbing a clean room cloth onto the grown chips and subsequently onto a clean  $\text{SiO}_2/\text{Si}^{++}$  substrate. This method does not involve solvents or other liquids which could effect the surface quality. These substrates are pre-patterned with gold markers to relocate individual flakes and enable consecutive electron beam lithography (EBL).

The flakes to be contacted are first chosen by optical microscopy and further characterized by AFM, which is also used to determine exact dimensions. The contacts are defined using standard EBL techniques and 5/50 nm Cr/Au ohmic contacts. Directly before metal evaporation the contact areas are etched for 15 s by oxygen plasma to remove any oxide layer from the  $\text{Bi}_2\text{Se}_3$  surface. This step is crucial for low contact resistances. The contact geometry of flakes with a high length/width ratio, resembles a fairly good approximation of a Hall bar geometry (*cf.* Figs. 2(a),(b)). With this method no additional patterning step is needed, allowing us to keep unetched flake edges, as grown in the VSS-process. The dimensions of the four investigated devices are summarized in Table I.

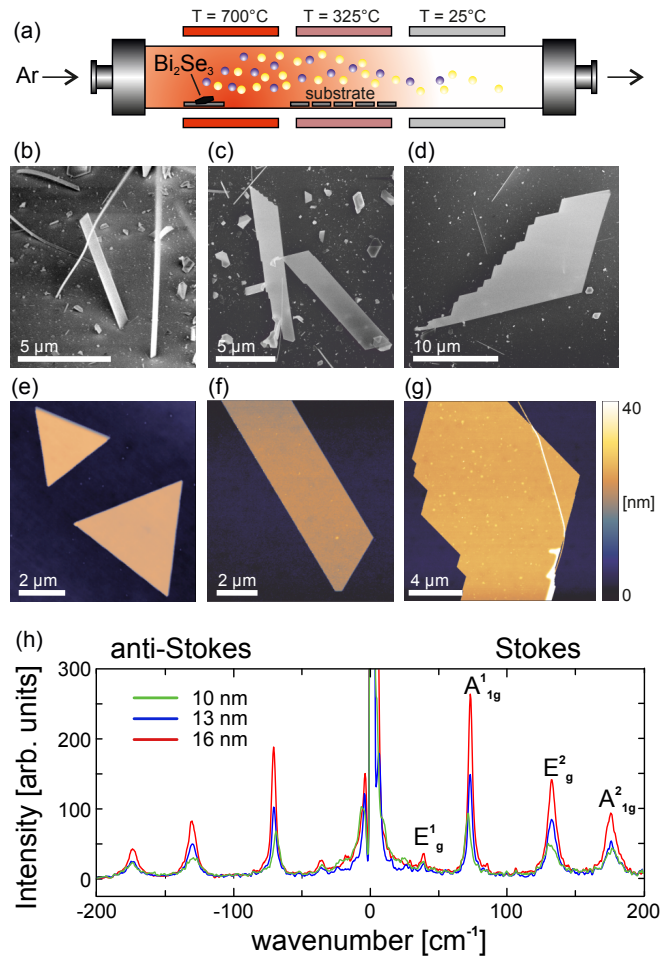


Figure 1. (color online) (a) Schematic illustration of the three-zone oven used for  $\text{Bi}_2\text{Se}_3$  sample growth. (b), (c) and (d) Scanning electron microscope images of typical ‘free standing’  $\text{Bi}_2\text{Se}_3$  ribbons and flakes. (e), (f) and (g) AFM images of grown flakes transferred onto  $\text{SiO}_2/\text{Si}$  substrate. (h) Characteristic Raman spectra of grown  $\text{Bi}_2\text{Se}_3$  flakes with different thicknesses.

### III. RESULTS AND DISCUSSION

Transport measurements were performed in a  $^4\text{He}$ -cryostat at a base temperature of  $T = 1.7$  K using low-frequency lock-in techniques. A superconducting solenoid, immersed in liquid Helium was used to apply magnetic fields perpendicular to the sample plane. The back gate characteristics of four different devices (see Fig. 2(b)) with different  $\text{Bi}_2\text{Se}_3$  crystal thickness are shown in Fig. 2(c) which depicts the four-terminal conductivity  $\sigma$  as function of applied back gate voltage  $V_g$ . For the 28 and 30 nm thick  $\text{Bi}_2\text{Se}_3$  samples almost no gate tunability is observed, which is in contrast to the two thinner (12 nm and 16 nm thick) samples where  $\sigma$  can be tuned by a factor of around 2. In none of our sam-

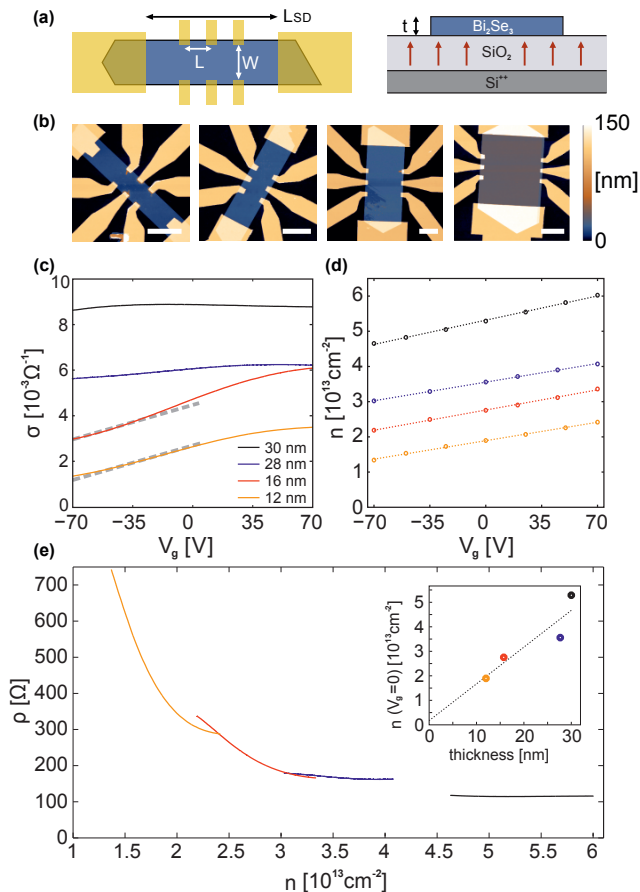


Figure 2. (color online) (a) Schematic illustrations of the sample geometry of contacted Bi<sub>2</sub>Se<sub>3</sub> flakes. In the left panel we highlight the width ( $W$ ), length ( $L$ ) and source-drain distance ( $L_{SD}$ ) of a contacted sample. The source-drain distance in our samples is in the range of 14 – 19 μm. Right panel shows a cross-section of our samples highlighting the flake with thickness ( $t$ ) resting on SiO<sub>2</sub> with back gate. (b) AFM images of the four investigated devices contacted with electrical contacts for Hall effect and magneto-resistance measurements. The scale bars are all 5 μm. For more details on the geometry please see Table I. (c) Conductivity as function of back gate voltage for all four samples. (d) Two-dimensional carrier density  $n$  of the different samples, extracted from the Hall resistance vs back gate voltages. (e) Resistivity as function of carrier density for all devices. The inset shows the carrier density at zero back gate voltage as function of Bi<sub>2</sub>Se<sub>3</sub> flake thickness.

ples we observe an ambipolar transport behavior, which is a first indication that very high n-doping of Bi<sub>2</sub>Se<sub>3</sub> is present in all our devices.

We performed Hall effect measurements to determine the charge carrier densities. The extracted two-dimensional (2D) electron density,  $n$ , which varies linearly with  $V_g$  is shown in Fig. 2(d) for all devices. The slope for the three thinner samples of 7.5 – 8.2 × 10<sup>10</sup> cm<sup>-2</sup>/V (see table 1) is in reasonably good agreement with the geometrical gate lever arm  $\alpha_g = \epsilon_0 \epsilon_r / (|e|d) \approx 7.2 \times 10^{10}$  cm<sup>-2</sup>/V, where  $d = 285$  nm is the

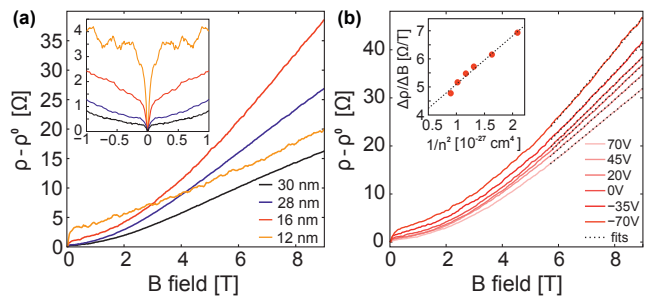


Figure 3. (color online) (a) Magneto-resistance  $\Delta\rho = \rho - \rho^0$  [where  $\rho^0 = \rho(B = 0 \text{ T})$ ] at zero back gate voltage for the four devices in Fig. 2. The inset shows WAL dips at small  $B$  fields. (b)  $\Delta\rho$  as function of  $B$ -field for the 16 nm thick sample for various back gate voltages (see labels). The inset shows the slopes of the linear magneto-resistance at high magnetic fields (see dashed lines in main panel) vs  $1/n^2$ .

thickness of the SiO<sub>2</sub> gate oxide with a dielectric constant of  $\epsilon_r \approx 4$ . From the vertical offsets of  $n$  in Fig. 2(d) we can estimate the average bulk charge carrier density. The inset in Fig. 2(e) shows the 2D carrier density  $n$  at zero gate voltage as function of the Bi<sub>2</sub>Se<sub>3</sub> crystal thickness. From the slope of this linear dependence (dotted line) we extract a 3D bulk carrier concentration of  $1.5 \times 10^{19}$  cm<sup>-3</sup> in our VSS Bi<sub>2</sub>Se<sub>3</sub> crystals. Finally, we plot the resistivity  $\rho = 1/\sigma$  of all four devices as function of  $n$  (main panel of Fig. 2(e)). The observed overall trend highlights a consistent carrier density dependency on the measured resistivity of all measured devices. The increasing gate tunability at lower carrier densities might be either connected (i) to the linear density of states of the 2D surface states or (ii) to a reduction of the 3D bulk density of states (or diffusion constant) at lower Fermi energy values. By assuming that surface states dominate the gate voltage dependence at low carrier densities we can estimate the carrier mobility from the nearly linear increase of  $\sigma$  as function of  $V_g$  (see dashed lines in Fig. 2(c)). From our data we extract respective surface carrier mobilities of  $\mu \approx 1600$  cm<sup>2</sup>(Vs)<sup>-1</sup>. As the condition  $\mu B > 1$  can be reached with experimentally accessible magnetic fields, Shubnikov-de Haas oscillations should become visible for  $B$ -fields larger than 5 T. We note, however, that we do not observe any Shubnikov-de Haas oscillations (see magneto-transport measurements below). We there-

device #	$t$ (nm)	$L$ (μm)	$W$ (μm)	$\alpha_g$ (cm <sup>-2</sup> V <sup>-1</sup> )
1	12	3.4	2.4	$7.5 \times 10^{10}$
2	16	3.5	2.9	$8.2 \times 10^{10}$
3	28	4.7	10.6	$7.5 \times 10^{10}$
4	30	3.5	11.8	$9.8 \times 10^{10}$

Table I. Geometrical dimensions of the four devices discussed. The dimensions are defined as in Fig. 2(a) and were measured using an AFM. The respective gate lever arms  $\alpha_g$  are also included.

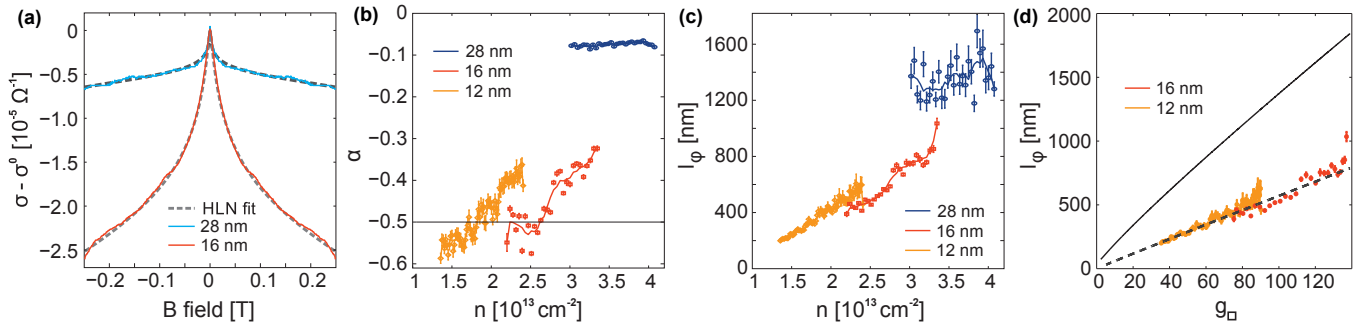


Figure 4. (color online) Weak antilocalization (WAL) peak in conductivity as function of  $B$  field (solid lines) and fits according the HLN model (dashed lines) for two different devices. (b), (c) Extracted fitting values for  $\alpha$  (panel b) and  $l_\phi$  (panel c) are shown as a function of the charge carrier density for three different devices. (d) Phase coherence length as function of the dimensionless conductivity  $g_\square$ . Here, the solid line displays the theoretical result by AAK [41]. The dashed line highlights the result modified due to a finite electron spin-flip scattering time  $\tau_{sf}$  (see text for details).

fore conclude that is very likely that transport in our samples is dominated by bulk transport, where the gate tunability originates from a Fermi level dependent 3D bulk density of states or diffusion constant.

For gaining more insights on the separation of bulk and surface transport we performed four-terminal magneto-resistance measurements (see Fig. 3(a)). The two most prominent features in our magneto-transport data are (i) a LMR at high magnetic fields [42–45] and (ii) a reasonably strong WAL dip at low magnetic fields (below 1 T) [44, 46–49], as shown by the inset of Fig. 3(a).

Above  $B = 5 - 6$  T all four devices exhibit LMR. Interestingly, the strength of the LMR does not solely depend on the sample thickness nor the total charge carrier density. We observe that the thinnest and thickest  $\text{Bi}_2\text{Se}_3$  crystal exhibit similar LMR slopes (see black and orange curves in Fig. 3(a)), whereas the other two devices (see red and blue curves in Fig. 3(a)) show a significantly larger slope of the LMR. However, within a single device we find a systematic carrier density dependence of the slope of the LMR at large magnetic fields (see Fig. 3(b)). A more detailed analysis of the carrier-density dependent LMR slope shows that, interestingly,  $\Delta\rho/\Delta B$  changes linearly as function of  $n^{-2}$  (see inset in Fig. 3(b)). This dependence is in agreement with the generic quantum description of galvanomagnetic phenomena by Abrikosov [50–52], leading to  $\rho \propto B/n^2$ . However, although for the investigated  $B$  field range the required condition  $\mu B > 1$  might be fulfilled, we are certainly not in the extreme quantum limit where only the lowest Landau level is filled. Moreover, it should be noted that the fit shown in the inset of Fig. 3(b) does not cross the origin. All these bring us to the conclusion that the LMR in our devices is rather dominated by the classical linear magneto-resistance [52] due to bulk inhomogeneities and defects in the  $\text{Bi}_2\text{Se}_3$  crystals which may also explain the high bulk carrier densities.

These findings are in contrast to the WAL, which exhibits a clear crystal thickness dependence (see inset of Fig. 3(a)) and which is therefore - also in agreement with

literature [48, 49, 53] - most likely a better fingerprint for surface state transport. WAL signatures are indeed inherent to the 2D states of TIs [3, 23, 46] As it is governed by quantum mechanical interference, a detailed investigation of resulting corrections to the conductance allows to learn more about phase coherent transport properties in these materials. Indeed, WAL in TIs has already been studied in great detail [54–57] and it has been shown that the so-called Hikami-Larkin-Nagaoka (HLN) model [58] can be used to fit the WAL corrections at low  $B$  fields. Within the HLN model the conductivity correction is expressed as

$$\Delta\sigma = \sigma(B) - \sigma(0) = -\frac{\alpha e^2}{2\pi^2\hbar} \left[ \ln\left(\frac{\hbar}{4Bel_\phi}\right) - \Psi\left(\frac{1}{2} + \frac{\hbar}{4Bel_\phi}\right) \right], \quad (1)$$

where  $\Psi$  is the digamma function and  $l_\phi$  is the phase coherence length. The value of the amplitude  $\alpha$  is expected to be  $-1/2$  for perfect WAL in a two-dimensional system. For an ideal 3D TI with two independent and decoupled 2D surfaces the expected value for the total WAL amplitude is therefore  $\alpha = -1$  [49]. For fitting our data, the symmetric and anti-symmetric part of the overall conductivity were separated. This is necessary considering the imperfect Hall bar geometry due to the etch-free sample fabrication process. Fig. 4(a) shows WAL data, fitted with the HLN model given by Eq. (1) for the symmetric part of the data with an additional term for quadratic magneto-resistance at low magnetic fields  $\beta B^2$ . The values for  $\alpha$  and  $l_\phi$  as extracted from the fits are shown in Figs. 4(b) and 4(c).

For the two thinner samples (orange and red data in Fig. 4(b))  $\alpha$  is gate tunable around a value of  $-1/2$ . This indicates that either the surface states are strongly coupled via the highly conductive bulk or that transport is purely dominated by the bulk. For the 28 nm thick sample (blue data in Figs. 4(b), 4(c)) no gate dependence is observed indicating the dominance of a bulk conduction channel with a Fermi level in a regime with constant

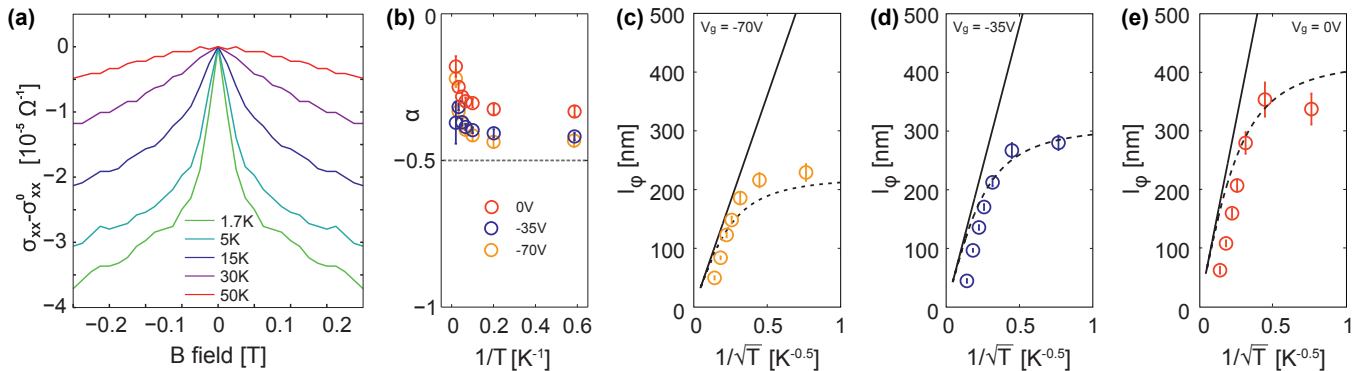


Figure 5. (color online) (a) Broadening of the WAL peak with increasing temperature for the 16 nm thick Bi<sub>2</sub>Se<sub>3</sub> sample. (b) Dependence of the parameter  $\alpha$  as a function of inverse temperature for different back gate voltages. (c), (d) and (e) Dependence of the phase coherence length  $l_\phi$  as a function of  $1/\sqrt{T}$  for three different back gate voltages. The solid and dashed lines resemble the same theoretical models as in Fig. 4(d).

3D bulk density of state which suppresses any gate tunability. The thickest sample (30 nm) does not show a distinct WAL peak and is hence excluded from our WAL analysis. A similar trend is also observed for the phase coherence length  $l_\phi$  which increases with larger sample thickness and increasing charge carrier density.

Interestingly, such a gate-tunable phase-coherence length - also observed by other groups [28, 59] - is in qualitative agreement with a scattering mechanism based on electron-electron interactions as predicted by Altshuler-Aronov-Khmelnitsky (AAK) for a two-dimensional system [41, 60]:

$$l_\phi = \hbar g_\square (4m^* k_B T \ln g_\square)^{-1/2}, \quad (2)$$

where  $k_B$  is the Boltzmann constant,  $m^*$  is the effective mass and  $g_\square = \sigma h/e^2$  is the dimensionless conductivity, which can be directly extracted from the measured conductivity. Apart from the small logarithmic correction (only becoming important for very small conductivities) the phase coherence length is a linear function of  $g_\square$ . By plotting the experimentally extracted  $l_\phi$  as function of  $g_\square$  (see Fig. 4(d)) we indeed can confirm this nearly linear dependence. Furthermore, by assuming a bulk carrier effective mass of  $m^* = 0.15m_e$  [61], we obtain the solid line in Fig. 4(d) without any further adjustable parameter. These values are a factor of 2 – 3 larger than the values of  $l_\phi$  extracted from our WAL measurements, meaning that there must be some corrections to the effective mass or (more likely) additional sources for dephasing.

This becomes even more apparent when investigating the temperature dependence of the WAL and the extracted  $l_\phi$  at different carrier densities, as shown in Fig. 5. In Fig. 5(a) we show the WAL peak for the 16 nm thick sample at different temperatures, highlighting its disappearing at elevated temperatures. The peak at small magnetic fields slowly decreases in amplitude completely disappears at 50 K. By fitting again the HNL model to our data we extract the temperature dependent  $\alpha$  values and phase-coherence lengths (Figs. 5(b)-5(e)). The

prefactor  $\alpha$  changes towards zero for increasing temperature, i.e. decreasing  $1/T$ , as seen in Fig. 5(b). More insights can be gained when investigating the temperature dependence of the phase coherence length. In order to highlight the expected temperature dependence given by Eq. 2 we plot  $l_\phi$  as function of  $1/\sqrt{T}$  in Figs. 5(c) to 5(e).

Similar to Fig. 4(d), the solid lines illustrate the estimates for  $l_\phi$  obtained from the AAK theory ( $l_\phi \propto 1/\sqrt{T}$ ) for different back gate voltages, i.e. carrier densities which are color coded in Figs. 5(c)-5(e). Indeed, above  $T = 7$  K (below  $1/\sqrt{T} \approx 0.4$  K<sup>-1/2</sup>), the experimentally extracted  $l_\phi$  values are inversely proportional to the square root of the temperature. However, at lower temperatures,  $l_\phi$  shows a carrier density dependent saturation behavior, which can not be explained by electron-electron interaction limiting the phase coherence length. To account for these discrepancies, we follow Ref. [60] and include an additional inelastic electron spin-flip scattering time,  $\tau_{sf}$ . Thus the phase coherence time  $\tau_\phi = l_\phi^2/D$  will be limited by  $\tau_{sf}$  at low temperatures. This leads to an overall scattering rate which is the sum of spin flip and the AAK decoherence rate,  $\tau_\phi^{-1} = \tau_{sf}^{-1} + k_B T \ln g_\square / (\hbar g_\square)$ . We use this expression to estimate  $l_\phi = \sqrt{D\tau_\phi}$ . By assuming a linear carrier density dependency of the spin flip scattering time  $\tau_{sf} = \beta n$  with  $\beta = 1.2 \times 10^{-24}$  cm<sup>2</sup>s, we obtain good agreement with all our experimental data (see dashed lines in Fig. 4(d) and Figs. 5(c) to (e)). The extracted  $\tau_{sf}$  values are on the order of 10 ps. This is a first experimental estimate of the spin flip scattering time in Bi<sub>2</sub>Se<sub>3</sub> from WAL data. The short timescale most likely results from the strong spin-orbit interaction in this material class [62]. We emphasize that the  $\tau_s$  value is not attributed to surface but rather to bulk transport properties.

#### IV. CONCLUSION

In conclusion, we used a catalyst-free vapor solid synthesis growth method for obtaining well-shaped single-crystalline  $\text{Bi}_2\text{Se}_3$  flakes with thicknesses in the range of a few nanometers. We performed low-temperature transport measurements on such  $\text{Bi}_2\text{Se}_3$  flakes with different layer thicknesses, resulting in different (two-dimensional) doping values. From magneto-transport measurements we extract information on the linear magneto-resistance as well as on phase coherent transport properties. In particular from weak antilocalization measurements we gain detailed insights on the phase-coherence length in bulk

transport. We observe that the phase-coherence length linearly depends on both the conductivity and electron density. Its values are close to the values imposed by electron-electron interaction but limited by spin-flip scattering at the lowest temperatures.

#### Acknowledgments

We gratefully acknowledge support from the Helmholtz nanoelectronic facility (HNF), the Helmholtz Virtual Institute of Topological insulators (VITI) and the DFG priority program SPP1666.

- 
- [1] B. A. Bernevig and S.-C. Zhang, “Quantum spin hall effect,” *Phys. Rev. Lett.*, vol. 96, p. 106802, Mar 2006.
- [2] L. Fu, C. L. Kane, and E. J. Mele, “Topological insulators in three dimensions,” *Phys. Rev. Lett.*, vol. 98, p. 106803, Mar 2007.
- [3] L. Fu and C. Kane, “Topological insulators with inversion symmetry,” *Phys. Rev. B*, vol. 76, no. 4, p. 045302, 2007.
- [4] J. E. Moore and L. Balents, “Topological invariants of time-reversal-invariant band structures,” *Phys. Rev. B*, vol. 75, p. 121306, Mar 2007.
- [5] X.-L. Qi, T. L. Hughes, and S.-C. Zhang, “Topological field theory of time-reversal invariant insulators,” *Phys. Rev. B*, vol. 78, p. 195424, Nov 2008.
- [6] D. Loss and D. P. DiVincenzo, “Quantum computation with quantum dots,” *Phys. Rev. A*, vol. 57, pp. 120–126, Jan 1998.
- [7] M. Z. Hasan and C. L. Kane, “Colloquium : Topological insulators,” *Rev. Mod. Phys.*, vol. 82, pp. 3045–3067, Nov 2010.
- [8] Z.-H. Pan, E. Vescovo, A. V. Fedorov, D. Gardner, Y. S. Lee, S. Chu, G. D. Gu, and T. Valla, “Electronic structure of the topological insulator  $\text{Bi}_2\text{Se}_3$  using angle-resolved photoemission spectroscopy: Evidence for a nearly full surface spin polarization,” *Phys. Rev. Lett.*, vol. 106, p. 257004, Jun 2011.
- [9] E. Majorana, “Teoria simmetrica dell’elettrone e del positrone,” *Il Nuovo Cimento (1924-1942)*, vol. 14, no. 4, pp. 171–184, 1937.
- [10] A. Y. Kitaev, “Unpaired majorana fermions in quantum wires,” *Physics-Uspekhi*, vol. 44, no. 10S, p. 131, 2001.
- [11] L. Fu and C. L. Kane, “Superconducting proximity effect and majorana fermions at the surface of a topological insulator,” *Phys. Rev. Lett.*, vol. 100, p. 096407, Mar 2008.
- [12] C. Beenakker, “Search for majorana fermions in superconductors,” *Condensed Matter Physics*, vol. 4, 2013.
- [13] H. Zhang, C. Liu, X. Qi, X. Dai, Z. Fang, and S. Zhang, “Topological insulators in  $\text{Bi}_2\text{Se}_3$ ,  $\text{Bi}_2\text{Te}_3$  and  $\text{Sb}_2\text{Te}_3$  with a single dirac cone on the surface,” *Nat. Phys.*, vol. 5, no. 6, pp. 438–442, 2009.
- [14] Y. Xia, D. Qian, D. Hsieh, L. Wray, A. Pal, H. Lin, A. Bansil, D. Grauer, Y. Hor, R. Cava, *et al.*, “Observation of a large-gap topological-insulator class with a single dirac cone on the surface,” *Nat. Phys.*, vol. 5, no. 6, pp. 398–402, 2009.
- [15] J. Kasparova, C. Drasar, A. Krejcova, L. Benes, P. Lostak, W. Chen, Z. Zhou, and C. Uher, “n-type to p-type crossover in quaternary  $\text{Bi}_x\text{Sb}_y\text{Pb}_z\text{Se}_3$  single crystals,” *Journal of applied physics*, vol. 97, no. 10, pp. 103720–103720, 2005.
- [16] D. O. Scanlon, P. D. C. King, R. P. Singh, A. de la Torre, S. M. Walker, G. Balakrishnan, F. Baumberger, and C. R. A. Catlow, “Controlling bulk conductivity in topological insulators: Key role of anti-site defects,” *Adv. Mater.*, vol. 24, no. 16, pp. 2154–2158, 2012.
- [17] G. Wang, X.-G. Zhu, Y.-Y. Sun, Y.-Y. Li, T. Zhang, J. Wen, X. Chen, K. He, L.-L. Wang, X.-C. Ma, *et al.*, “Topological insulator thin films of  $\text{Bi}_2\text{Te}_3$  with controlled electronic structure,” *Advanced Materials*, vol. 23, no. 26, pp. 2929–2932, 2011.
- [18] Y. Yan, Z.-M. Liao, Y.-B. Zhou, H.-C. Wu, Y.-Q. Bie, J.-J. Chen, J. Meng, X.-S. Wu, and D.-P. Yu, “Synthesis and quantum transport properties of  $\text{Bi}_2\text{Se}_3$  topological insulator nanostructures,” *Scientific Reports*, vol. 3, 2013.
- [19] K. Novoselov, D. Jiang, F. Schedin, T. Booth, V. Khotkevich, S. Morozov, and A. Geim, “Two-dimensional atomic crystals,” *Proceedings of the National Academy of Sciences of the United States of America*, vol. 102, no. 30, pp. 10451–10453, 2005.
- [20] K. Novoselov, A. Geim, S. Morozov, D. Jiang, M. Grigorieva, S. Dubonos, and A. Firsov, “Two-dimensional gas of massless dirac fermions in graphene,” *Nature*, vol. 438, no. 7065, pp. 197–200, 2005.
- [21] Y. Zhang, K. He, C. Chang, C. Song, L. Wang, X. Chen, J. Jia, Z. Fang, X. Dai, W. Shan, *et al.*, “Crossover of the three-dimensional topological insulator  $\text{Bi}_2\text{Se}_3$  to the two-dimensional limit,” *Nat. Phys.*, vol. 6, no. 8, pp. 584–588, 2010.
- [22] G. Zhang, H. Qin, J. Chen, X. He, L. Lu, Y. Li, and K. Wu, “Growth of topological insulator  $\text{Bi}_2\text{Se}_3$  thin films on  $\text{SrTiO}_3$  with large tunability in chemical potential,” *Adv. Funct. Mater.*, vol. 21, no. 12, pp. 2351–2355, 2011.
- [23] J. Chen, H. Qin, F. Yang, J. Liu, T. Guan, F. Qu, G. Zhang, J. Shi, X. Xie, C. Yang, *et al.*, “Gate-voltage control of chemical potential and weak antilocalization in  $\text{Bi}_2\text{Se}_3$ ,” *Phys. Rev. Lett.*, vol. 105, no. 17, p. 176602, 2010.
- [24] D. Kong, J. C. Randel, H. Peng, J. J. Cha, S. Meister, K. Lai, Y. Chen, Z.-X. Shen, H. C. Manoharan, and

- Y. Cui, "Topological insulator nanowires and nanoribbons," *Nano Lett.*, vol. 10, no. 1, pp. 329–333, 2010.
- [25] H. Peng, K. Lai, D. Kong, S. Meister, Y. Chen, X.-L. Qi, S.-C. Zhang, Z.-X. Shen, and Y. Cui, "Aharonov-Bohm interference in topological insulator nanoribbons," *Nat. Mater.*, vol. 9, no. 3, pp. 225–229, 2010.
- [26] B. F. Gao, P. Gehring, M. Burghard, and K. Kern, "Gate-controlled linear magnetoresistance in thin  $\text{Bi}_2\text{Se}_3$  sheets," *Appl. Phys. Lett.*, vol. 100, no. 21, pp. –, 2012.
- [27] L. Alegria, M. Schroer, A. Chatterjee, G. Poirier, M. Pretko, S. Patel, and J. Petta, "Structural and electrical characterization of  $\text{Bi}_2\text{Se}_3$  nanostructures grown by metal-organic chemical vapor deposition," *Nano Lett.*, vol. 12, no. 9, pp. 4711–4714, 2012.
- [28] H. Steinberg, J.-B. Laloë, V. Fatemi, J. S. Moodera, and P. Jarillo-Herrero, "Electrically tunable surface-to-bulk coherent coupling in topological insulator thin films," *Phys. Rev. B*, vol. 84, no. 23, p. 233101, 2011.
- [29] J. Krumrain, G. Mussler, S. Borisova, T. Stoica, L. Plucinski, C. Schneider, and D. Grützmacher, "MBE growth optimization of topological insulator  $\text{Bi}_2\text{Te}_3$  films," *J. Cryst. Growth*, vol. 324, no. 1, pp. 115–118, 2011.
- [30] N. V. Tarakina, S. Schreyeck, T. Borzenko, C. Schumacher, G. Karczewski, K. Brunner, C. Gould, H. Buhmann, and L. W. Molenkamp, "Comparative study of the microstructure of  $\text{Bi}_2\text{Se}_3$  thin films grown on  $\text{Si}(111)$  and  $\text{InP}(111)$  substrates," *Crystal Growth & Design*, vol. 12, no. 4, pp. 1913–1918, 2012.
- [31] S. Borisova, J. Krumrain, M. Luysberg, G. Mussler, and D. Grützmacher, "Mode of growth of ultrathin topological insulator  $\text{Bi}_2\text{Te}_3$  films on  $\text{Si}(111)$  substrates," *Crystal Growth & Design*, vol. 12, no. 12, pp. 6098–6103, 2012.
- [32] D. Kong, W. Dang, J. J. Cha, H. Li, S. Meister, H. Peng, Z. Liu, and Y. Cui, "Few-layer nanoplates of  $\text{Bi}_2\text{Se}_3$  and  $\text{Bi}_2\text{Te}_3$  with highly tunable chemical potential," *Nano Lett.*, vol. 10, no. 6, pp. 2245–2250, 2010.
- [33] H. Li, J. Cao, W. Zheng, Y. Chen, D. Wu, W. Dang, K. Wang, H. Peng, and Z. Liu, "Controlled synthesis of topological insulator nanoplate arrays on mica," *J. Am. Chem. Soc.*, vol. 134, no. 14, pp. 6132–6135, 2012.
- [34] P. Gehring, B. F. Gao, M. Burghard, and K. Kern, "Growth of high-mobility  $\text{Bi}_2\text{Te}_2\text{Se}$  nanoplatelets on hbn sheets by van der Waals epitaxy," *Nano Lett.*, vol. 12, no. 10, pp. 5137–5142, 2012.
- [35]  $\text{Bi}_2\text{Se}_3$  from Alfa Aesar, Vacuum Deposition Grade, 99.999%.
- [36] K. M. F. Shahil, M. Z. Hossain, V. Goyal, and A. A. Balandin, "Micro-Raman spectroscopy of mechanically exfoliated few-quintuple layers of  $\text{Bi}_2\text{Te}_3$ ,  $\text{Bi}_2\text{Se}_3$  and  $\text{Sb}_2\text{Te}_3$  materials," *J. Appl. Phys.*, vol. 111, no. 5, p. 054305, 2012.
- [37] N. H. Tu, Y. Tanabe, K. K. Huynh, Y. Sato, H. Oguro, S. Heguri, K. Tsuda, M. Terauchi, K. Watanabe, and K. Tanigaki, "Van der Waals epitaxial growth of topological insulator  $\text{Bi}_{2-x}\text{Sb}_x\text{Te}_3\text{Se}_y$  ultrathin nanoplate on electrically insulating fluorophlogopite mica," *Applied Physics Letters*, vol. 105, no. 6, p. 063104, 2014.
- [38] B. Guo, Q. Liu, E. Chen, H. Zhu, L. Fang, and J. R. Gong, "Controllable n-doping of graphene," *Nano Letters*, vol. 10, no. 12, pp. 4975–4980, 2010.
- [39] W. Richter and C. Becker, "A Raman and far-infrared investigation of phonons in the rhombohedral  $\text{V}_2\text{-VI}_3$  compounds  $\text{Bi}_2\text{Te}_3$ ,  $\text{Bi}_2\text{Se}_3$ ,  $\text{Sb}_2\text{Te}_3$  and  $\text{Bi}_2(\text{Te}_{1-x}\text{Se}_x)_3$  ( $0 < x < 1$ ),  $(\text{Bi}_{1-y}\text{Sb}_y)_2\text{Te}_3$  ( $0 < y < 1$ )," *physica status solidi (b)*, vol. 84, no. 2, pp. 619–628, 1977.
- [40] J. Zhang, Z. Peng, A. Soni, Y. Zhao, Y. Xiong, B. Peng, J. Wang, M. S. Dresselhaus, and Q. Xiong, "Raman spectroscopy of few-quintuple layer topological insulator  $\text{Bi}_2\text{Se}_3$  nanoplatelets," *Nano Letters*, vol. 11, no. 6, pp. 2407–2414, 2011.
- [41] B. L. Altshuler, A. G. Aronov, and D. E. Khmel'nitsky, "Effects of electron-electron collisions with small energy transfers on quantum localization," *Journal of Physics C: Solid State Physics*, vol. 15, no. 36, p. 7367, 1982.
- [42] H. Tang, D. Liang, R. L. Qiu, and X. P. Gao, "Two-dimensional transport-induced linear magneto-resistance in topological insulator  $\text{Bi}_2\text{Se}_3$  nanoribbons," *ACS Nano*, vol. 5, no. 9, pp. 7510–7516, 2011.
- [43] H. He, B. Li, H. Liu, X. Guo, Z. Wang, M. Xie, and J. Wang, "High-field linear magneto-resistance in topological insulator  $\text{Bi}_2\text{Se}_3$  thin films," *Appl. Phys. Lett.*, vol. 100, no. 3, p. 032105, 2012.
- [44] S.-P. Chiu and J.-J. Lin, "Weak antilocalization in topological insulator  $\text{Bi}_2\text{Te}_3$  microflakes," *Phys. Rev. B*, vol. 87, p. 035122, Jan 2013.
- [45] Y. Yan, L.-X. Wang, D.-P. Yu, and Z.-M. Liao, "Large magnetoresistance in high mobility topological insulator  $\text{Bi}_2\text{Se}_3$ " *Applied Physics Letters*, vol. 103, no. 3, p. 033106, 2013.
- [46] H.-Z. Lu and S.-Q. Shen, "Weak localization of bulk channels in topological insulator thin films," *Phys. Rev. B*, vol. 84, no. 12, p. 125138, 2011.
- [47] H.-Z. Lu, J. Shi, and S.-Q. Shen, "Competition between weak localization and antilocalization in topological surface states," *Phys. Rev. Lett.*, vol. 107, p. 076801, Aug 2011.
- [48] Y. S. Kim, M. Brahlek, N. Bansal, E. Edrey, G. A. Kapilevich, K. Iida, M. Tanimura, Y. Horibe, S.-W. Cheong, and S. Oh, "Thickness-dependent bulk properties and weak antilocalization effect in topological insulator  $\text{Bi}_2\text{Se}_3$ " *Phys. Rev. B*, vol. 84, no. 7, p. 073109, 2011.
- [49] D. Kim, P. Syers, N. P. Butch, J. Paglione, and M. S. Fuhrer, "Coherent topological transport on the surface of  $\text{Bi}_2\text{Se}_3$ " *Nature communications*, vol. 4, 2013.
- [50] A. Abrikosov, "Galvanomagnetic phenomena in metals in the quantum limit," *Soviet Journal of Experimental and Theoretical Physics*, vol. 29, p. 746, 1969.
- [51] A. Abrikosov, "Quantum linear magnetoresistance; solution of an old mystery," *Journal of Physics A: Mathematical and General*, vol. 36, p. 9119, 2003.
- [52] J. Hu and T. Rosenbaum, "Classical and quantum routes to linear magnetoresistance," *Nat. Mater.*, vol. 7, no. 9, pp. 697–700, 2008.
- [53] N. Bansal, Y. S. Kim, M. Brahlek, E. Edrey, and S. Oh, "Thickness-independent transport channels in topological insulator  $\text{Bi}_2\text{Se}_3$  thin films," *Phys. Rev. Lett.*, vol. 109, no. 11, p. 116804, 2012.
- [54] A. Taskin, S. Sasaki, K. Segawa, and Y. Ando, "Manifestation of topological protection in transport properties of epitaxial  $\text{Bi}_2\text{Se}_3$  thin films," *Phys. Rev. Lett.*, vol. 109, no. 6, p. 066803, 2012.
- [55] J. Checkelsky, Y. Hor, R. Cava, and N. Ong, "Bulk band gap and surface state conduction observed in voltage-tuned crystals of the topological insulator  $\text{Bi}_2\text{Se}_3$ " *Phys. Rev. Lett.*, vol. 106, no. 19, p. 196801, 2011.
- [56] H.-T. He, G. Wang, T. Zhang, I.-K. Sou, G. K. Wong, J.-N. Wang, H.-Z. Lu, S.-Q. Shen, and F.-C. Zhang, "Im-

- purity effect on weak antilocalization in the topological insulator  $\text{Bi}_2\text{Te}_3$ ” *Phys. Rev. Lett.*, vol. 106, no. 16, p. 166805, 2011.
- [57] J. J. Cha, D. Kong, S.-S. Hong, J. G. Analytis, K. Lai, and Y. Cui, “Weak antilocalization in  $\text{Bi}_2(\text{Se}_x\text{Te}_{1-x})_3$  nanoribbons and nanoplates,” *Nano Lett.*, vol. 12, no. 2, pp. 1107–1111, 2012.
- [58] S. Hikami, A. I. Larkin, and Y. Nagaoka, “Spin-orbit interaction and magnetoresistance in the two dimensional random system,” *Progress of Theoretical Physics*, vol. 63, no. 2, pp. 707–710, 1980.
- [59] L. A. Jauregui, M. T. Pettes, L. P. Rokhinson, L. Shi, and Y. P. Chen, “Gate tunable relativistic mass and berry’s phase in topological insulator nanoribbon field effect devices,” *arXiv preprint arXiv:1402.2659*, 2014.
- [60] S. Engels, B. Terrés, A. Epping, T. Khodkov, K. Watanabe, T. Taniguchi, B. Beschoten, and C. Stampfer, “Limitations to carrier mobility and phase-coherent transport in bilayer graphene,” *Physical review letters*, vol. 113, no. 12, p. 126801, 2014.
- [61] M. Orlita, B. Piot, G. Martinez, N. S. Kumar, C. Faugeras, M. Potemski, C. Michel, E. Hankiewicz, T. Brauner, Č. Drašar, *et al.*, “Magneto-optics of massive dirac fermions in bulk  $\text{Bi}_2\text{Se}_3$ ” *Physical Review Letters*, vol. 114, no. 18, p. 186401, 2015.
- [62] D. Pesin and A. H. MacDonald, “Spintronics and pseudospintronics in graphene and topological insulators,” *Nature Materials*, vol. 11, p. 409, 2012.